Chaos, Solitons and Fractals 200 (2025) 117162

Contents lists available at ScienceDirect

Chaos, Solitons and Fractals

journal homepage: www.elsevier.com/locate/chaos

Escape and transport in chaotic motion of charged particles in a magnetized plasma under the influence of two and three modes of drift waves

P. Haerter [a,*], R.L. Viana [a,b], E.D. Leonel [c]

[a] Departamento de Física, Universidade Federal do Paraná, Curitiba, 81531-990, Paraná, Brazil
[b] Centro Interdisciplinar de Ciência, Tecnologia e Inovação, Núcleo de Modelagem e Computação Científica, Universidade Federal do Paraná, Curitiba, 81531-990, Paraná, Brazil
[c] Departamento de Física, Universidade Estadual Paulista, Rio Claro, 13506-900, São Paulo, Brazil

ARTICLE INFO

Keywords:
Plasma transport
Escape basins
Tokamaks
Hamiltonian plasma
Anomalous transport

ABSTRACT

This study investigates how two- and three-wave configurations govern particle escape and transport in tokamak edge plasmas. Using a Hamiltonian model derived from drift-wave turbulence, we analyze test particle dynamics through Poincaré maps, fractal escape basins, and entropy metrics. Introducing a third wave increases basin entropy, enhancing particle escape rates while reducing basin boundary entropy, indicative of suppressed basin mixing. Escape time analyses reveal resonant scattering disrupts coherent transport pathways, linking fractal absorption patterns to heat load mitigation in divertors. Characteristic transport is also analyzed and regimes transition between anomalous ($\alpha > 1$) and normal diffusion ($\alpha \approx 1$), two-wave systems sustain anomalous transport, while the third wave homogenizes fluxes through stochastic scattering. Fractal structures in escape basins and entropy-driven uncertainty quantification suggest strategies to engineer transport properties, balancing chaos and order for optimized confinement.

1. Introduction

The confinement of high-temperature plasmas in magnetic fusion devices remains a critical challenge due to the interplay of turbulent fluctuations and anomalous particle transport [1–4]. Drift waves, driven by density and temperature gradients in magnetized plasmas, generate turbulent electric fields that induce chaotic particle motion [5]. This motion results in particle escape rates that far exceed predictions from classical collisional theory [6,7]. Such anomalous transport degrades plasma performance and risks damaging reactor walls through localized heat and particle fluxes, necessitating advanced mitigation strategies [8–12].

Particle transport in high-temperature plasmas is dominated by long-range electric fields arising from Coulomb interactions among charged particles. In magnetized plasmas, low-frequency ion acoustic oscillations emerge as critical collective modes, governing transport properties such as resistivity and thermal conductivity. Steep density and temperature gradients trigger instabilities in these modes, leading to drift-wave turbulence and consequent anomalous transport of particles and energy [7,9,13].

Among the various instabilities in tokamaks, electrostatic drift-wave turbulence in the plasma edge plays a pivotal role in governing cross-field transport [1]. These low-frequency fluctuations, driven by steep density and temperature gradients, generate turbulent electric fields that drive $\mathbf{E} \times \mathbf{B}$ drifts—a key mechanism for chaotic particle motion [14,15].

* Corresponding author.
E-mail address: haerter@ufpr.br (P. Haerter).

https://doi.org/10.1016/j.chaos.2025.117162
Received 24 June 2025; Received in revised form 27 August 2025; Accepted 29 August 2025
Available online 11 September 2025
0960-0779/© 2025 Elsevier Ltd. All rights are reserved, including those for text and data mining, AI training, and similar technologies.

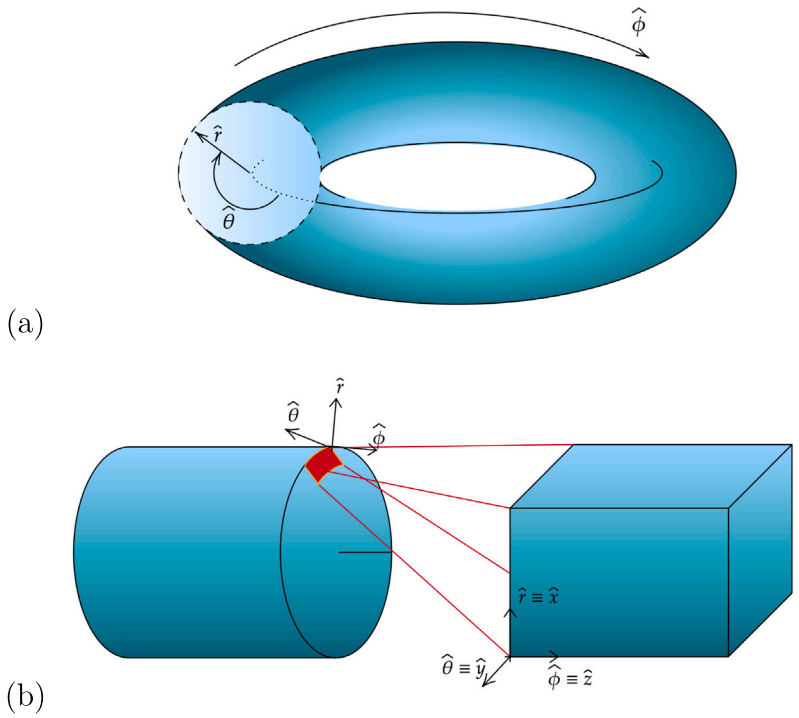


Fig. 1. Graphical representation of the (a) toroidal geometry and the (b) transformation of cylindrical coordinates to rectangular ones.

A typical framework for analyzing these dynamics is the Horton model [16], which reduces the plasma edge to a slab geometry with a uniform magnetic field $\mathbf{B} = B\hat{z}$. Particle motion is described through $\mathbf{E}\times\mathbf{B}$ drifts governed by a Hamiltonian formulated from electrostatic potentials. By decomposing the potential into an equilibrium component ($\Phi_0(x)$) and perturbative contributions from N drift waves, this model predicts the emergence of fractal structures in phase space, where chaotic and quasi-regular trajectories intertwine.

Recent studies [17,18] demonstrate how drift-wave turbulence generates fractal escape basins regions of initial conditions leading to particle loss characterized by self-similar patterns and Wada boundaries. In these boundaries, three or more basins share a common fractal edge, a feature critical for understanding particle migration toward plasma-facing components such as divertors [19–21]. Here, fractal absorption patterns directly influence heat and particle load distributions, complicating efforts to optimize reactor durability. The transition from integrable to chaotic dynamics under varying wave configurations further challenges confinement, as resonant interactions between modes amplify stochasticity and disrupt coherent transport pathways.

Quantitative tools such as basin entropy (S_b) and basin boundary entropy (S_{bb}) [22] have emerged to characterize the uncertainty and fractality of escape processes. These metrics reveal how perturbations amplify unpredictability in particle trajectories, even in systems with seemingly uniform chaotic regions. For instance, in tokamaks with ergodic magnetic limiters, fractal basins persist despite attempts to homogenize heat loads, highlighting the intrinsic complexity of plasma-wall interactions [17,23]. Reduced fractal dimensions correlate with elevated anomalous diffusion exponents, suggesting plasma edge turbulence alters transport via analogous mechanisms [8].

This paper extends prior work by analyzing how two- and three-wave configurations alter escape and transport regimes in magnetized plasmas. The manuscript is structured as follows: Section 2 outlines the theoretical model and numerical framework; Section 3 details particle escape dynamics and its impact on trajectory uncertainty across perturbation ranges; Section 4 presents transport analyses across periodic and chaotic regimes, contrasting diffusion behaviors under varying wave amplitudes; and Section 5 summarizes key conclusions and implications for plasma confinement.

2. Drift-Waves model

A well-known model for describing the influence of electrostatic potential turbulence caused by drift waves in the plasma edge is the one proposed by Horton [16]. Neglecting curvature effects, the plasma edge region can be approximated by a slab geometry. We therefore transform the toroidal coordinates (r, θ, ϕ) into a Cartesian system (x, y, z), as illustrated in Fig. 1. Here, x corresponds to the radial direction, y represents the poloidal direction (with periodicity 2π), and z denotes the toroidal direction. The uniform magnetic field is expressed as $\mathbf{B} = B\hat{z}$.

We assume that the ion and electron charges do not appreciably affect the electric and magnetic fields; hence, the corresponding guiding centers can be considered as passive tracers, or test particles. Such test particles move with the $\mathbf{E}\times\mathbf{B}$ drift velocity.

$$\mathbf{v} = -\frac{\nabla\Phi\times\mathbf{B}}{B^2}, \tag{1}$$

where the electric field is written as $\mathbf{E} = -\nabla\Phi$, with $\Phi(x, y, t)$ being a scalar potential. This system is equivalent to the following set of canonical equations:

$$v_x = \frac{\mathrm{d}x}{\mathrm{d}t} = -\frac{1}{B_0}\frac{\partial\Phi}{\partial y}, \tag{2}$$

$$v_y = \frac{\mathrm{d}y}{\mathrm{d}t} = \frac{1}{B_0}\frac{\partial\Phi}{\partial x}, \tag{3}$$

corresponding to the time-dependent Hamiltonian

$$H(x, y, t) = \frac{1}{B_0}\Phi(x, y, t). \tag{4}$$

The electric potential can be divided into two parts: an equilibrium part $\Phi_0(x)$ corresponding to a radial electric field, and a perturbation caused by N drift waves with amplitudes A_i, frequencies ω_i, and wave vectors $\mathbf{k}_i = (k_{x,i}, k_{y,i})$ for $i = 1, 2, \ldots, N$. This gives:

$$\Phi(x, y, t) = \Phi_0(x) + \sum_{i=1}^{N} A_i \sin(k_{x,i}x)\cos(k_{y,i}y - \omega_i t), \tag{5}$$

where we assume a stationary wave pattern along the radial direction x and a traveling wave along the poloidal direction y. Let L_x and L_y be the characteristic lengths along these directions, such that:

$$k_x = \frac{n\pi}{L_x}, \qquad k_y = \frac{2\pi m}{L_y}, \tag{6}$$

where m and n are suitably chosen positive integers.

In the case of N drift waves, the Hamiltonian reads:

$$H(x, y, t) = \frac{1}{B_0}[\Phi_0(x) + \sum_{i=1}^{N} A_i \sin(k_{x,i}x)\cos(k_{y,i}y - \omega_i t)]. \tag{7}$$

After transitioning to a reference frame moving with the phase velocity of the first wave, u_1, and considering the resonant case where the drift velocity satisfies

$$v_e = \frac{1}{B}\frac{\mathrm{d}\Phi_0}{\mathrm{d}x} = u_1 = \frac{\omega_1}{k_{y,1}},$$

the Hamiltonian becomes:

$$H(x, y, t) = A_1 \sin(k_{x,1}x)\cos(k_{y,1}y) + \sum_{i=2}^{N} A_i \sin(k_{x,i}x + \beta_i)\cos\big(k_{y,i}(y - u_i t)\big), \tag{8}$$

where $u_i = \frac{\omega_i}{k_{y,i}} - \frac{\omega_1}{k_{y,1}}$ and β_i is a phase term associated with the breakdown of transport barriers in symmetry regions. This phase enables particle transport along the x-direction, which is the focus of this study [24].

Considering two and three modes in the Hamiltonian equation (8), we evolved the canonical Eqs. (2) and (3) numerically from $t_i = 0$ to $t_f = 10^4$. A Poincaré map was constructed by sampling (x, y) values at times equal to integer multiples of the period $T = 2\pi/\omega_1$. The system parameters are defined as follows:

$$k_{x,1} = 5, \quad k_{y,1} = 6, \quad \omega_1 = 2, \quad A_1 = 1.0,$$
$$k_{x,2} = -3, \quad k_{y,2} = -3, \quad \omega_2 = 2, \quad A_2 \in [0, 1.0],$$
$$k_{x,3} = -2, \quad k_{y,3} = -3, \quad \omega_3 = 2, \quad A_3 = 0.1.$$

These values were chosen to reflect realistic plasma wave dynamics [13,25–27], with A_2 (the amplitude of the second wave) serving as a tunable parameter in the range $[0.0, 1.0]$. The integrable case $A_2 = A_3 = 0$ is shown in Fig. 2(a), where particle motion is confined to bounded cells.

By using a Poincaré map, we observe the patterns of particle motion by leveraging the periodicity of the stroboscopic mapping. This is achieved by sampling the coordinates (x, y) for each particle at times $t_n = nT$, where $T = 2\pi/u_1$ is the period of the parent wave. Fig. 2 illustrates the resulting maps for different values of A_2. Analysis reveals that increasing the control parameter A_2 triggers the destruction of invariant curves near displaced elliptic points, leading to a consequent enlargement of chaotic orbits. The persistence of periodic orbits at higher A_2 values arises from the choice of k_x and k_y, which correspond to smaller wavelengths. These wavelengths slow the destruction of KAM tori, preserving quasi-regular motion in localized regions.

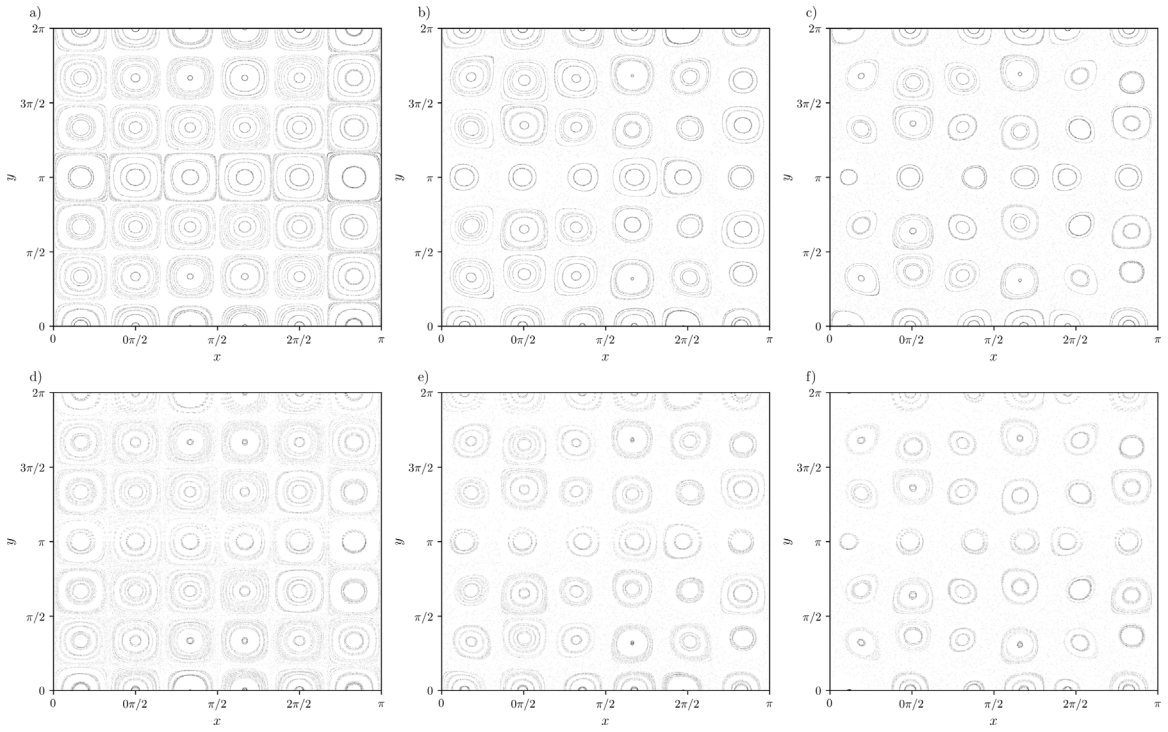


Fig. 2. Phase space for two configurations: the first row corresponds to $A_3 = 0$, and the second row to $A_3 = 0.1$. Columns represent different A_2 values: (a,d) 0.0, (b,e) 0.5, and (c,f) 0.9.

On the other hand, the addition of the third wave with $A_3 = 0.1$ (Fig. 2(d)) breaks the integrability of the system. In this case, only the interior of the cells retains quasiperiodic motion, unlike the two-wave scenario studied earlier [17]. The inclusion of the third wave accelerates the destruction of quasiperiodic islands due to the cumulative effect of multiple perturbations in the integrable system. This results in slightly more chaotic orbits in phase space and enhances particle transport, a phenomenon we will analyze in detail later.

3. Escape basins

The dynamics presented in Fig. 2 are aperiodic but not uniformly chaotic due to the intricate structure of the underlying manifolds [17]. This non-uniformity in chaotic motion can be quantified through the geometry of escape basins. Here, "escape" or "leaking" [28,29], is defined as particles exiting the $L_x \times L_y$ domain, which physically corresponds to migration into distinct plasma regions: the plasma-wall boundary for $x > \pi$ or the plasma core for $x < 0$. Initial conditions not residing in chaotic regions (e.g., those within periodic islands) produce non-escaping orbits and are excluded from exit basins.

Fig. 3 shows the exit basins for the wall (blue-colored regions) and the core (yellow-colored regions). Initial conditions that never escape are represented as blank areas. The exit basins exhibit an intricate structure for all values of the control parameter A_2. The comparable size of the basins across most A_2 values indicates no preferential escape direction (Fig. 4(a)). However, this symmetry can be broken by modulating the equilibrium potential profile $\Phi_0(x)$, as demonstrated in prior work [18].

The inclusion of the third wave with a small amplitude is linked to a physically interesting phenomenon in plasma physics [11,13,14,30–32]. While its effects are hardly perceived by direct comparison of exit basins in Fig. 3, we quantify the basin areas by calculating the fraction of basin points relative to the total number of grid points dividing the phase portrait. By comparing the sizes of the two basins for each case (Fig. 4a), it is evident that the third wave causes more particles to escape, with an increase of approximately 3%. The positive trend in all escape basins with increasing A_2 can be attributed to the enlargement of chaotic orbits. This expansion increases the number of initial conditions available for trajectories that eventually escape to either boundary.

To measure the impact of different exit configurations, we utilize basin entropy analysis [22]. This framework operates by dividing a region of interest, Ω, in the phase space into a uniform grid of boxes, each with a linear dimension ε. For a given parameter set, there exist two potential exits from Ω. This allows for the construction of a map, $C : \Omega \to \mathbb{N}$, which assigns a specific exit to every initial condition. This assigned exit is commonly referred to as a "color".

Theoretically, every box contains an infinite number of trajectories, each corresponding to one of the two colors. In any practical application, however, only a finite number of trajectories can be tracked for each box. This number reflects the repetitions in an experiment or the quantity of trajectories computed in a simulation.

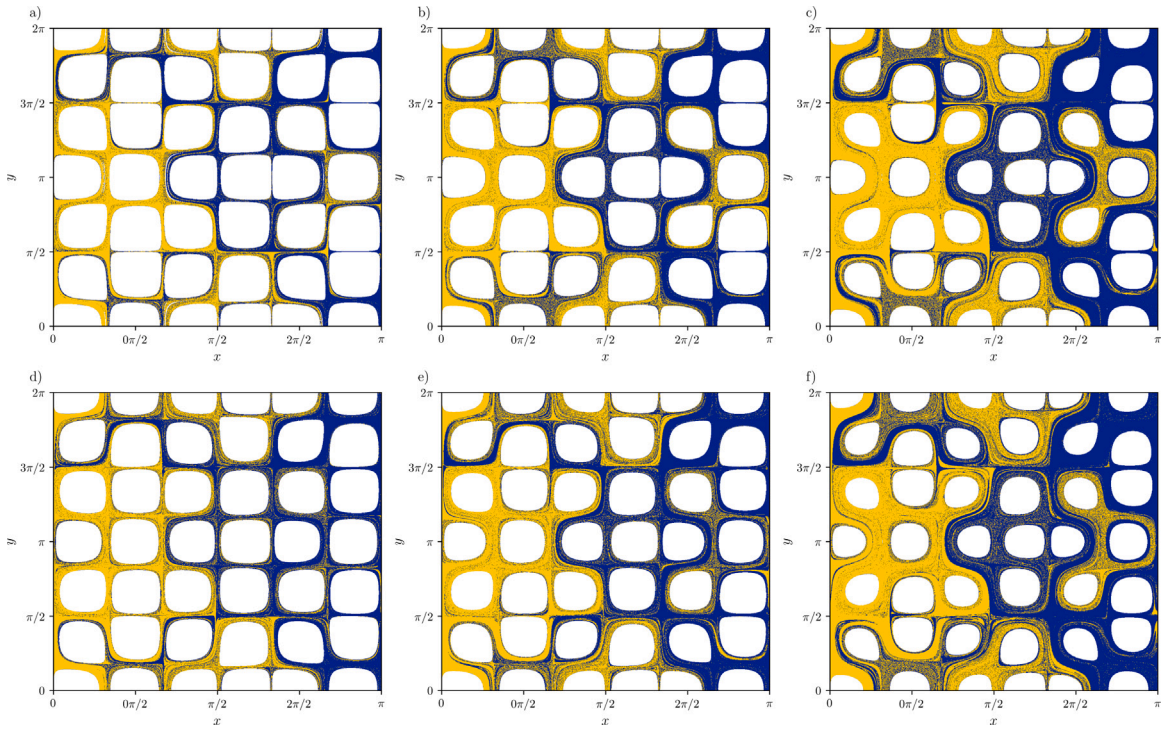


Fig. 3. Escape basins for the core ($x < 0$, yellow regions) and the wall ($x > \pi$, blue regions). The first row corresponds to the system with only the second wave ($A_3 = 0$), while the second row includes the third wave ($A_3 = 0.1$). The perturbation amplitudes of the second wave are: (a, (d) $A_2 = 0.3$, (b, (e) $A_2 = 0.5$, and (c, (f) $A_2 = 0.9$. (For interpretation of the references to color in this figure legend, the reader is referred to the web version of this article.)

For our computational analysis, we established a grid of 256×256 boxes across the phase space. We sampled this space using a total of 1024×1024 initial conditions, which corresponds to sixteen trajectories originating from within each box. This density of initial conditions was chosen as it provides a reliable estimation of the basin entropy while maintaining computational efficiency, consistent with previous studies [22]. Consequently, the linear size of each box, ε, which sets our analysis's resolution limit, is $1/256$.

Even with a resolution limit of ε, the trajectory data from within a single box can be used to quantify the local uncertainty. We can model the distribution of colors within a box as stochastic. An observed frequency, $p_{i,j}$, is then associated with each color j in a box i. This value is determined by the statistical outcomes of the trajectories that start inside that box.

Assuming that the trajectories within a box are statistically independent, the Gibbs entropy for an individual box i is calculated as:

$$S_i = -\sum_{j=1}^{m_i} p_{i,j} \log p_{i,j}, \tag{9}$$

where m_i is the number of distinct colors found in box i. Since the system has only two exits, m_i can be either 1 (for a box belonging to a single basin) or 2 (for a box on the basin boundary). The term $p_{i,j}$ represents the fraction of trajectories from that box that lead to exit j.

The total entropy, S, for the entire grid of N non-overlapping boxes that covers Ω is the summation of the entropies from each box:

$$S = \sum_{i=1}^{N} S_i. \tag{10}$$

To establish a measure that is independent of the grid resolution (and therefore the number of boxes), the basin entropy, S_b, is defined by normalizing the total entropy. This results in the average entropy per box:

$$S_b = \frac{S}{N}. \tag{11}$$

This framework can be extended to create more specialized metrics. For example, one might need to analyze the uncertainty concentrated at the boundaries between basins, which is useful for determining if a boundary is fractal. To do this, the entropy calculation is restricted to only the N_b boxes that contain more than one color. This defines the boundary basin entropy, S_{bb}, as:

$$S_{bb} = \frac{S}{N_b}, \tag{12}$$

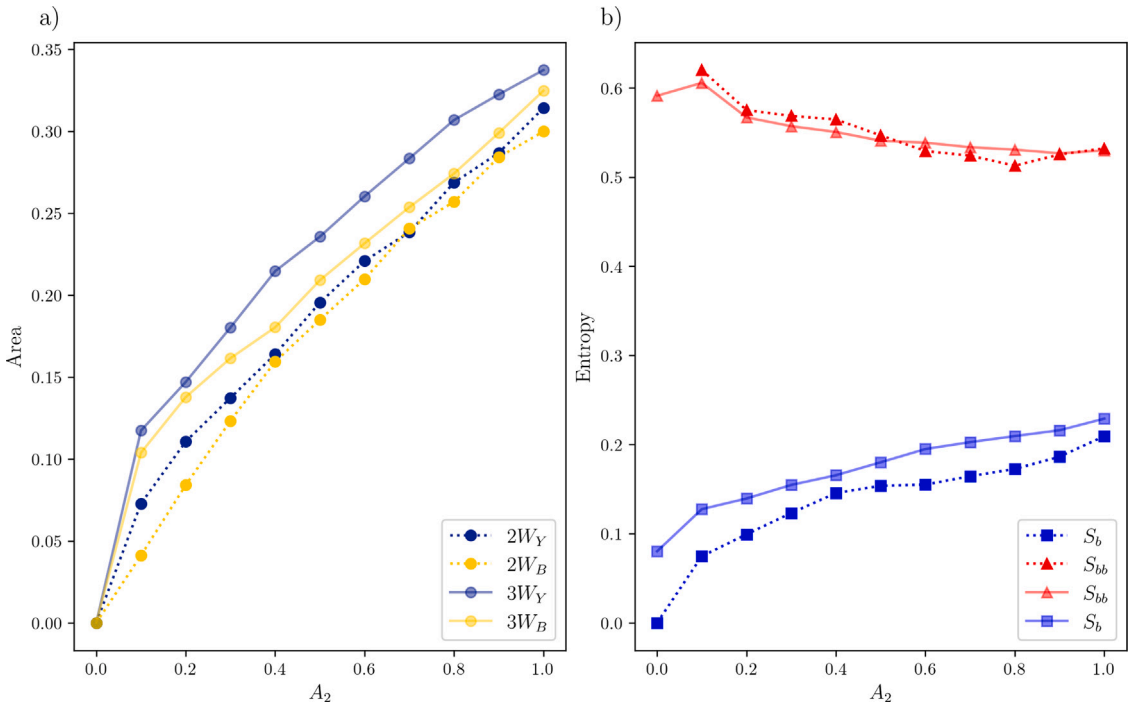


Fig. 4. Analysis for two-wave (2 W, dotted line) and three-wave (3 W, solid line) systems across varying second-wave perturbation amplitudes A_2. Panel (a) shows the fraction of the occupied area, where the legend subscripts Y and B refer to the escape basins for the core (yellow) and the wall (blue), respectively. Panel (b) displays the basin entropy and basin boundary entropy for both cases. (For interpretation of the references to color in this figure legend, the reader is referred to the web version of this article.)

This metric specifically quantifies the uncertainty present at the basin boundaries.

These two metrics can analyze the complexity, mixing, and uncertainty of initial conditions within escape basins or basins of attraction. They are closely linked to established metrics like the fractal dimension of attractors and the uncertainty exponent [33,34]. While the fractal dimension is excellent for quantifying the geometric complexity of basin boundaries, a topic we explored in prior work [17,18], we selected basin entropy here as it provides a more direct measure of the unpredictability of a particle final destination. When $S_b \to 0$, nearly all initial conditions within a small box of size ε^2 converge to the same exit, reflecting minimal uncertainty and higher trajectory predictability. Conversely, when $S_b \to \ln N_A$, initial conditions within the box are distributed equally among all exits, indicating maximal uncertainty and unpredictability.

Fig. 4(b) displays the basin entropy and basin boundary entropy for both analyzed cases. As expected, the results show that the basin entropy increases with larger values of the second wave's amplitude (A_2). This increase arises from enhanced chaotic behavior in the system, which amplifies the fractality and structural complexity of the basins.

When comparing the basin entropy S_b, the three-wave case exhibits higher values for all A_2, including a nonzero S_b at $A_2 = 0.0$. This nonzero entropy arises from the breaking of invariant curves due to the third wave, which ensures the system always exhibits escape basins. This is further corroborated by the presence of basin boundary entropy (S_{bb}) even at $A_2 = 0.0$. The basin entropy values are consistently higher in the presence of the third wave, demonstrating that even a small additional perturbation disrupts basin mixing and amplifies uncertainty.

The S_{bb}, on the other hand, presents a lower value when the third wave is added. This is counterintuitive but expected: while the third wave increases mixing in the system (producing more boundary points), the basin boundary entropy S_{bb} decreases because the averaging denominator N_b (number of mixed-attractor boxes) grows faster than the sum of entropies. The negative trend in S_{bb} arises as the escape regions expand. With both core and wall basins growing proportionally, the occupied area increases, but the uncertainty grows only marginally. Meanwhile, the rise in N_b reflects a larger number of mixed-attractor regions, diluting S_{bb} despite the heightened structural complexity.

Furthermore, it is also possible to analyze the escape time of particles for different second-wave amplitudes. Fig. 5 illustrates this relationship, where warmer colors correspond to longer escape times and cooler colors indicate faster-escaping particles. The fast-escape regions correlate with smooth basin boundaries, a consequence of unstable manifolds in the system and reduced divergence among initial conditions.

Conversely, regions with prolonged escape times are associated with sticky orbits. These are trajectories that become transiently trapped in the chaotic layer surrounding the KAM islands of quasi-regular motion before escaping. This phenomenon is characteristic of Hamiltonian systems and is visually confirmed by the concentration of long escape times (warmer colors in Fig. 5) at the frontiers of the non-escaping regions (white areas in Fig. 3).

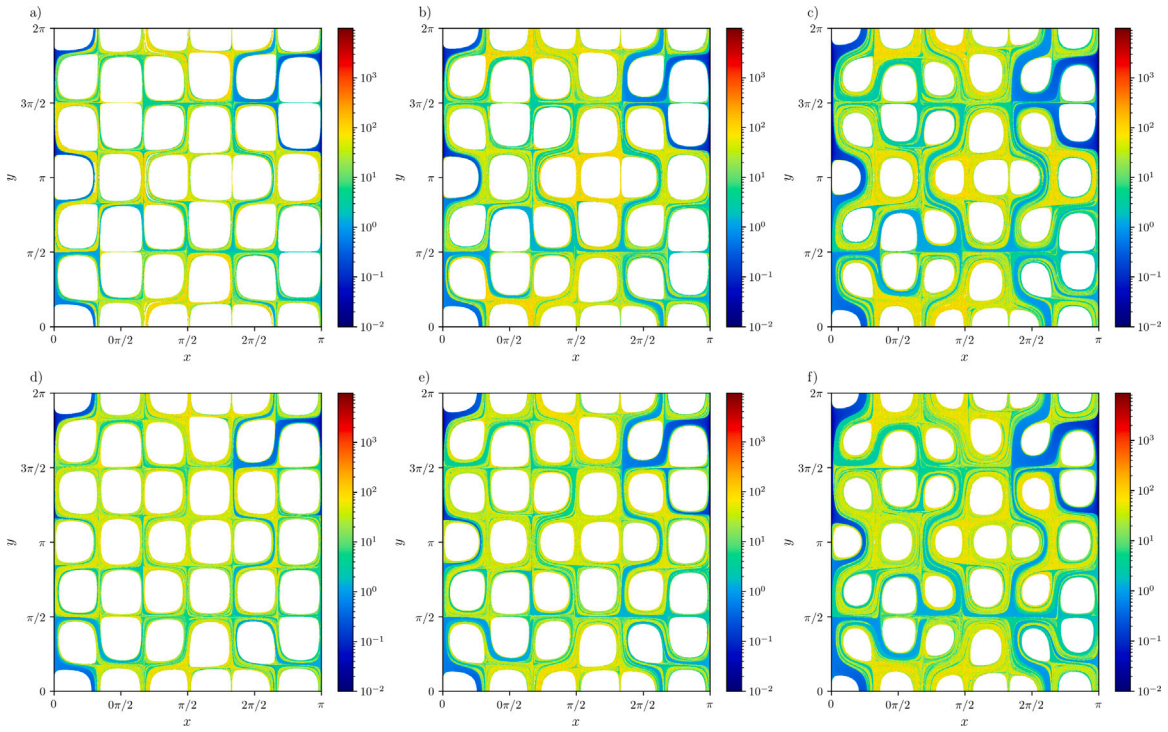


Fig. 5. Escape time for particles in two configurations: the first row corresponds to the system with only the second wave ($A_3 = 0$), while the second row includes the third wave ($A_3 = 0.1$). Columns represent different second-wave perturbation amplitudes: (a, (d) $A_2 = 0.3$, (b, (e) $A_2 = 0.5$, and (c, (f) $A_2 = 0.9$. Warmer colors indicate longer escape times, while cooler colors denote faster escapes. (For interpretation of the references to colour in this figure legend, the reader is referred to the web version of this article.)

4. Particle transport

To analyze the transport dynamics induced by the presence of two and three waves, we simulated an ensemble of passive particles initially distributed within the same region studied for escape basin characterization.

We employed diagnostic measures to quantify how distinct wave configurations influence particle transport in tokamaks. Specifically, we calculated two metrics: the mean square displacement (MSD), which provides a global characterization of chaotic transport by quantifying the spatial spread of particles over time, and the total displacement, which captures the inhomogeneous nature of transport due to spatially varying flux intensities across plasma regions.

4.1. Mean square displacement

For a statistical characterization of transport, we computed the mean square displacement (MSD):

$$\langle \sigma(t)^2 \rangle = \frac{1}{N} \sum_{i=1}^{N} ()|\mathbf{x}_i(t) - \mathbf{x}_i(0)|^2, \tag{13}$$

where N denotes the total number of particles. The temporal scaling exponent $\langle \sigma(t)^2 \rangle \propto t^{\alpha}$ classifies the transport regime as subdiffusive ($\alpha < 1$), normal diffusion ($\alpha = 1$), superdiffusive ($1 < \alpha < 2$), or ballistic ($\alpha = 2$).

Our analysis reveals two distinct regimes of anomalous transport, characterized by different scaling exponents (α), which emerge as a direct consequence of the waves' presence. Despite similar escape characteristics, two- and three-wave systems induce markedly different transport dynamics. In the two-wave case, particles exhibit enhanced poloidal transport, leading to spatially heterogeneous high-flux regions. Conversely, the addition of a third wave suppresses these localized transport channels due to resonant interactions, resulting in nearly constant diffusion across parameter space and effective poloidal confinement. This resonance mechanism homogenizes transport fluxes, reducing overall system transport compared to the two-wave scenario. The Fig. 6 summarizes the MSD scaling across the parameter space for the two and three wave, revealing a clear distinction between two groups: one corresponding to two waves system (Blue curve) and the three waves (Red curve).

The observed diffusion exponent provides a quantitative measure of the transport regimes and their underlying mechanisms. The anomalous diffusion regime observed for the two-wave system suggests the formation of highly correlated regions where particles exhibit persistent directional coherence. This behavior mirrors coherent structures in plasma turbulence, such as zonal flows or

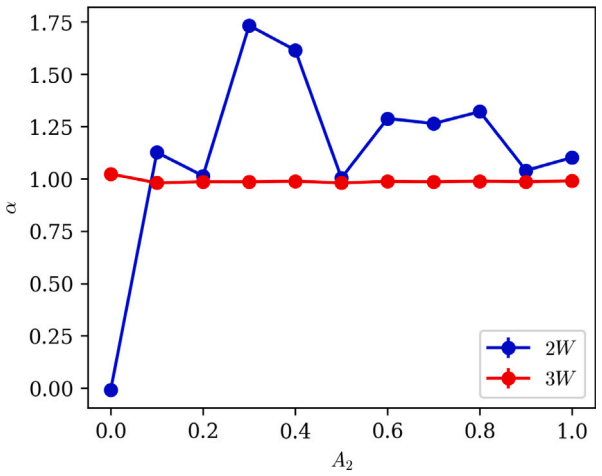


Fig. 6. Mean square displacement (MSD) of particles for two- and three-wave systems at multiple values of the second wave perturbation amplitude ($A_2 \in [0.0, 1.0]$). The results highlight the confinement effect induced by the third wave and the nonlinear dependence of displacement on A_2 in the two-wave case. (For interpretation of the references to color in this figure legend, the reader is referred to the web version of this article.)

streamers, which efficiently channel particles along preferential pathways. This phenomenon stems from the two waves generating localized high-transport channels within the chaotic sea. However, as the second wave amplitude (A_2) increases, the amplified chaotic dynamics disrupt these channels—reducing periodic orbits and suppressing transport efficiency.

In contrast, the normal diffusion regime under three waves indicates a structured phase space without the formation of high-transport regions. Here, directional coherence – which drives localized transport – is suppressed by the third wave. This suppression arises because the third wave introduces resonant interactions that amplify background stochasticity, trapping particles in transient coherent structures or inducing frequent scattering. These mechanisms disrupt anomalous-diffusion pathways, homogenizing transport and preventing large-scale particle flux.

4.2. Total displacement

The total displacement of particles (Δ) is defined as the Euclidean distance between their initial and final positions:

$$\Delta = \sqrt{(\Delta x)^2 + (\Delta y)^2}, \tag{14}$$

providing critical insights into both the magnitude and directionality of transport. Unlike the mean square displacement (MSD), which quantifies particle dispersion, the total displacement highlights net migration of particles. By analyzing Δ alongside directional displacements (Δx, Δy), we observe two distinct regimes identified in the MSD analysis: localized high-transport regions in the two-wave system, where particles exhibit coherent motion, and diffuse transport in the three-wave system, where the third wave disrupts directional coherence.

The total displacement Δ is consistent with the scaling exponent α in the MSD analysis. By comparing displacements across spatial regions, we identified areas of enhanced transport. These regions correlate with chaotic dynamics in phase space, while suppressed transport aligns with quasi-regular orbits trapped near invariant structures.

Fig. 7 illustrates the displacement patterns observed for different wave configurations. The first row corresponds to the two-wave system ($A_3 = 0$), while the second row shows the three-wave system ($A_3 = 0.1$). Columns are ordered by increasing second-wave perturbation amplitude: $A_2 = 0.3$, $A_2 = 0.5$, and $A_2 = 0.9$ (left to right).

The displacement metric reinforces the separation of transport regimes observed in Fig. 6. For the two-wave system (first row of Fig. 7), the total displacement reveals distinct dynamics: particles travel farther when the scaling exponent α is higher (e.g., $A_2 = 0.3$), with localized high-transport regions near $(1.0, \pi)$. However, these regions are suppressed as the wave amplitude (A_2) increases. Conversely, in cases where $\alpha \approx 1$, the displacement exhibits similar behavior across parameters, with no high-transport structures forming. Chaotic regions instead display isotropic displacement due to frequent scattering, which suppresses net migration by trapping particles in transient structures. This scattering arises from both the increased second-wave amplitude and the presence of the third wave, hindering the formation of structured transport pathways.

Our conclusions are not strictly limited to the parameters chosen in this study. The qualitative behaviors we describe are general features of this wave-interaction model, and similar transport dynamics have been observed using different parameter sets [35]. The essential condition for these phenomena is a mixed phase space where chaotic and regular motion coexist, which occurs over a broad range of wave amplitudes.

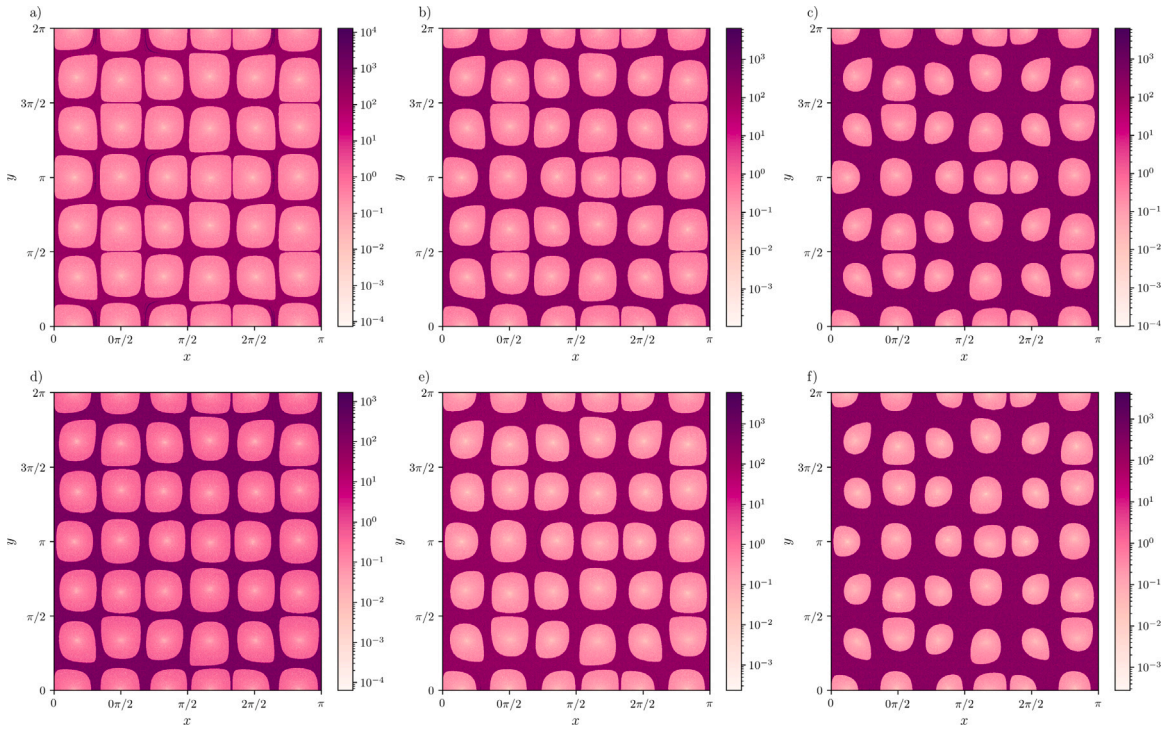


Fig. 7. Total displacement (Δ) of advected particles. The first row corresponds to the two-wave system ($A_3 = 0$), and the second row includes the third wave ($A_3 = 0.1$). Columns represent different second-wave perturbation amplitudes: (a, (d) $A_2 = 0.3$, (b, (e) $A_2 = 0.5$, and (c, (f) $A_2 = 0.9$.

5. Conclusions

This work investigates the role of drift-wave modes in governing particle escape and transport dynamics in tokamak edge plasmas. By comparing systems with two and three waves, we demonstrate how the introduction of a third wave modifies uncertainty and transport regimes.

The addition of a third wave increases the overall particle escape by approximately 3%. The underlying dynamical changes also lead to an increase in the basin entropy S_b, reflecting greater unpredictability in particle destinations. Concurrently, the basin boundary entropy S_{bb} is generally reduced, which can be attributed to how this metric averages uncertainty over an increasing number of mixed boundary boxes. This suggests that while overall escape is enhanced and general phase-space unpredictability (S_b) rises, the complexity specifically at the basin boundaries (as measured by S_{bb}) shows a constrained behavior. Auxiliary diagnostics, including escape time and phase-space trajectory analyses, corroborate these results, revealing suppressed coherent transport pathways under three-wave configurations. The interplay between enhanced overall escape, increased general unpredictability, and this constrained nature of boundary complexity underscores the potential of multi-wave turbulence control for optimizing plasma confinement strategies.

The suppression effect of the third wave extends to transport dynamics. Systems with two drift waves exhibit anomalous diffusion ($\alpha > 1$), driven by high transport regions that channel particles along preferential pathways. In contrast, the third wave disrupts these pathways through resonant scattering, restoring normal diffusion ($\alpha \approx 1$) and homogenizing transport fluxes. This duality highlights the delicate balance between order and chaos in multi-wave plasmas, with profound implications for confinement optimization and divertor design. By suppressing anomalous transport while maintaining confinement efficiency, controlled wave interactions offer a pathway to stabilize particle motion and reduce heat loads on reactor walls.

These results bridge fundamental plasma turbulence studies to practical confinement challenges. The observed fractal structures in escape basins, coupled with the tunable transition between anomalous and normal diffusion, suggest that multi-wave configurations could be engineered to tailor transport properties. Future work should explore scaling these findings to realistic reactor geometries and experimental validation of entropy-based control strategies.

CRediT authorship contribution statement

P. Haerter: Writing – review & editing, Writing – original draft, Visualization, Validation, Software, Project administration, Methodology, Investigation, Formal analysis, Data curation, Conceptualization. **R.L. Viana:** Writing – review & editing, Writing – original draft, Supervision, Project administration, Investigation, Funding acquisition, Formal analysis, Conceptualization. **E.D. Leonel:** Writing – review & editing, Visualization, Supervision, Methodology, Formal analysis.

Declaration of competing interest

The authors declare that they have no known competing financial interests or personal relationships that could have appeared to influence the work reported in this paper.

Acknowledgments

This work has been supported by grants from the Brazilian Government Agencies CNPq and CAPES. P. Haerter received partial financial support from the following Brazilian government agencies: CNPq (140920/2022-6), CAPES (88887.898818/2023-00). E.D.Leonel acknowledges support from Brazilian agencies CNPq (No. 301318/2019-0, 304398/2023-3) and FAPESP (No. 2019/14038-6 and No. 2021/09519-5). R. L. Viana received partial financial support from the following Brazilian government agencies: CNPq (403120/2021-7, 301019/2019-3), CAPES (88881.143103/2017-01).

Data availability

No data was used for the research described in the article.

References

[1] Diamond PH, Itoh S-I, Itoh K, Hahm TS. Zonal flows in plasma—a review. Plasma Phys Control Fusion 2005;47(5):R35. http://dx.doi.org/10.1088/0741-3335/47/5/R01.
[2] Chen FF. Introduction to Plasma Physics and Controlled Fusion. Cham: Springer International Publishing; 2016, http://dx.doi.org/10.1007/978-3-319-22309-4.
[3] Hazeltine RD, Meiss JD. Plasma Confinement. Courier Corporation; 2013.
[4] Balescu R. Transport Processes in Plasmas. North-Holland; 1988.
[5] Camargo SJ, Scott BD, Biskamp D. The influence of magnetic fluctuations on collisional drift-wave turbulence. Phys Plasmas 1996;3(11):3912–31. http://dx.doi.org/10.1063/1.871580.
[6] Garbet X, Mantica P, Angioni C, Asp E, Baranov Y, Bourdelle C, Budny R, Crisanti F, Cordey G, Garzotti L, Kirneva N, Hogeweij D, Hoang T, Imbeaux F, Joffrin E, Litaudon X, Manini A, McDonald DC, Nordman H, Parail V, Peeters A, Ryter F, Sozzi C, Valovic M, Tala T, Thyagaraja A, Voitsekhovitch I, Weiland J, Weisen H, Zabolotsky A, Contributors TJE. Physics of transport in tokamaks. Plasma Phys Control Fusion 2004;46(12B):B557–74. http://dx.doi.org/10.1088/0741-3335/46/12B/045.
[7] Wagner F, Stroth U. Transport in toroidal devices-the experimentalist's view. Plasma Phys Control Fusion 1993;35(10):1321. http://dx.doi.org/10.1088/0741-3335/35/10/002.
[8] Balescu R. Aspects of anomalous transport in plasmas. Boca Raton: CRC Press; 2005, http://dx.doi.org/10.1201/9780367801601.
[9] Horton W. Drift waves and transport. Rev Modern Phys 1999;71(3):735–78. http://dx.doi.org/10.1103/RevModPhys.71.735.
[10] Horton W. Turbulent Transport in Magnetized Plasmas. 2nd ed.. WORLD SCIENTIFIC; 2017, http://dx.doi.org/10.1142/10595.
[11] Katou K. Resonant three-wave interaction in electrostatic drift-wave turbulence. J Phys Soc Japan 1982;51(3):996–1000. http://dx.doi.org/10.1143/JPSJ.51.996.
[12] Nordman H, Weiland J, Jarmén A. Simulation of toroidal drift mode turbulence driven by temperature gradients and electron trapping. Nucl Fusion 1990;30(6):983. http://dx.doi.org/10.1088/0029-5515/30/6/001.
[13] Batista AM, Caldas IL, Lopes SR, Viana RL, Horton W, Morrison PJ. Nonlinear three-mode interaction and drift-wave turbulence in a tokamak edge plasma. Phys Plasmas 2006;13(4):042510. http://dx.doi.org/10.1063/1.2184291.
[14] Hasegawa A, Mima K. Pseudo-three-dimensional turbulence in magnetized nonuniform plasma. Phys Fluids 1978;21(1):87–92. http://dx.doi.org/10.1063/1.862083.
[15] Scott BD. Energetics of the interaction between electromagnetic ExB turbulence and zonal flows. New J Phys 2005;7(1):92. http://dx.doi.org/10.1088/1367-2630/7/1/092.
[16] Horton W. Onset of stochasticity and the diffusion approximation in drift waves. Plasma Phys Control Fusion 1985;27(9):937. http://dx.doi.org/10.1088/0741-3335/27/9/001.
[17] Mathias AC, Viana RL, Kroetz T, Caldas IL. Fractal structures in the chaotic motion of charged particles in a magnetized plasma under the influence of drift waves. Phys A 2017;469:681–94. http://dx.doi.org/10.1016/j.physa.2016.11.049.
[18] Viana RL, Mathias AC, Marcus FA, Kroetz T, Caldas IL. Fractal boundaries in chaotic Hamiltonian systems. J Phys: Conf Ser 2017;911(1):012002. http://dx.doi.org/10.1088/1742-6596/911/1/012002.
[19] Loarte A. Effects of divertor geometry on tokamak plasmas. Plasma Phys Control Fusion 2001;43:R183.
[20] Zweben SJ, Ellis RA, Titus P, Xing A, Zhang H. Rapidly moving divertor plates in a tokamak. Fusion Sci Technol 2011;60:197–202.
[21] Ivanova-Stanik I, Chmielewski P, Day C, Innocente P, Zagórski R. Divertor power spreading in the divertor tokamak test facility for a full power scenario with Ar and Ne seeding. Plasma Phys Control Fusion 2023;65:055009.
[22] Daza A, Wagemakers A, Georgeot B, Guéry-Odelin D, Sanjuán MAF. Basin entropy: A new tool to analyze uncertainty in dynamical systems. Sci Rep 2016;6(1):31416. http://dx.doi.org/10.1038/srep31416.
[23] Haerter P, de Souza LC, Mathias AC, Viana RL, Caldas IL. Basin entropy and wada property of magnetic field line escape in toroidal plasmas with reversed shear. Int J Bifurc Chaos 2023;33(09):2330022. http://dx.doi.org/10.1142/S0218127423300227.
[24] Kleva RG, Drake JF. Stochastic E×B particle transport. Phys Fluids 1984;27(7):1686–98. http://dx.doi.org/10.1063/1.864823.
[25] Heller MVAP, Castro RM, Caldas IL, Brasílio ZA, Silva RPd, Nascimento IC. Correlation between plasma edge electrostatic and magnetic oscillations in the Brazilian Tokamak TBR. J Phys Soc Japan 1997;66(11):3453–60. http://dx.doi.org/10.1143/JPSJ.66.3453.
[26] Castro RM, Heller MVAP, Caldas IL, da Silva RP, Brasilio ZA, Nascimento IC. Temperature fluctuations and plasma edge turbulence in the Brazilian tokamak TBR. Phys Plasmas 1996;3(3):971–7. http://dx.doi.org/10.1063/1.871802.
[27] dos Santos Lima GZ, Guimarães-Filho ZO, Batista AM, Caldas IL, Lopes SR, Viana RL, Nascimento IC, Kuznetsov YK. Bicoherence in electrostatic turbulence driven by high magnetohydrodynamic activity in Tokamak Chauffage Alfvén Brésilien. Phys Plasmas 2009;16(4):042508. http://dx.doi.org/10.1063/1.3099701.
[28] Schneider J, Tél T, Neufeld Z. Dynamics of "Leaking" Hamiltonian systems. Phys Rev E: Stat Phys Plasmas, Fluids, Related Interdiscip Top 2002;66:066218.

[29] Bleher S, Grebogi C, Ott E, Brown R. Fractal boundaries for exit in Hamiltonian dynamics. Phys Rev A 1988;38(2):930–8. http://dx.doi.org/10.1103/PhysRevA.38.930.
[30] Horton W, Hasegawa A. Quasi-two-dimensional dynamics of plasmas and fluids. Chaos: An Interdiscip J Nonlinear Sci 1994;4(2):227–51. http://dx.doi.org/10.1063/1.166049.
[31] Waltz RE. Three-dimensional numerical simulations of simple electron drift wave turbulence in a sheared and curved magnetic field. Phys Fluids B: Plasma Phys 1990;2(9):2118–34. http://dx.doi.org/10.1063/1.859432.
[32] Leoncini X, Agullo O, Benkadda S, Zaslavsky GM. Anomalous transport in Charney-Hasegawa-Mima flows. Phys Rev E: Stat Phys Plasmas, Fluids, Related Interdiscip Top 2005;72(2):026218. http://dx.doi.org/10.1103/PhysRevE.72.026218.
[33] Daza A, Wagemakers A, Sanjuán MAF. Classifying basins of attraction using the basin entropy. Chaos Solitons Fractals 2022;159:112112. http://dx.doi.org/10.1016/j.chaos.2022.112112.
[34] Ott E. Chaos in Dynamical Systems. 2nd ed.. Cambridge: Cambridge University Press; 2002, http://dx.doi.org/10.1017/CBO9780511803260.
[35] Bósio AF, Caldas IL, Viana RL, Elskens Y. Identifying ballistic modes via Poincaré sections. Commun Nonlinear Sci Numer Simul 2025;145:108722. http://dx.doi.org/10.1016/j.cnsns.2025.108722.